Type and Species Selective Air Etching of Single Walled Carbon Nanotubes Studied with *In Situ* Raman Spectroscopy

Andrew Li-Pook-Than [†‡], *Jacques Lefebvre* [†] *and Paul Finnie* *[†‡]

[†]Institute for Microstructural Sciences, National Research Council Canada, Building M-50, 1200 Montreal Road, Ottawa, ON, K1A 0R6, Canada and [‡]Department of Physics, University of Ottawa, 150 Louis Pasteur, Ottawa, ON, K1N 6N5, Canada

Supporting Information (19 pp.)

Diameter and chirality assignment for Radial Breathing Mode and G- peaks. Raman spectra of sample etched at T = 600°C. Radial Breathing Mode time evolution plots. This material is available free of charge via the Internet at http://pubs.acs.org.

1. Diameter and chirality assignment

A standard way to determine the (n,m) of single walled carbon nanotubes (SWNTs) is to use the so called Kataura plot. In the Kataura plot, the Raman laser energy is displayed on the y-axis, while the measured Radial Breathing Mode (RBM) frequency is on the x-axis. Because the RBM frequency is roughly inversely proportional to nanotube diameter, and because RBM visibility depends on being resonant with laser energy, with the resonances being chirality dependent, each nanotube has a specific

position on the Kataura plot. In essence, each SWNT chirality (n,m) is assigned to different ω_{RBM} and E_{ii} pairs.

In this work, Kataura plots are obtained using data from R. Saito's Exciton Kataura Plot page (i.e. http://flex.phys.tohoku.ac.jp/eii/).[1, 2]

Assignment may not be straightforward because RBM frequencies shift weakly and resonance energies (i.e. E_{11}, E_{22}, etc.) shift strongly under different nanotube environments. Specifically, these pairings can be sensitive to a dielectric function κ, which depends on local environment and nanotube diameter.[1] Furthermore, we are using a fixed wavelength laser so observation of an RBM means the laser is "near" the resonant frequency (i.e. within ~100 meV), but we do not determine the exact resonance (i.e. position on the y-axis of the Kataura plot).[3]

In Table S1, we list the room temperature RBMs shown in Figure 3. Our aim is to assign these to specific species.

A simple model of the diameter dependence of the RBM frequency is $\omega_{RBM} = A/d_t + B$, where A and B are constants that depend on local environment and sample type. This has often been used to assign experimental RBM peaks; different values for A and B have been obtained in different studies.[4-7] Since our samples were grown under water-assisted CVD on Si subtrate, we expect A to vary between 227 nm·cm^{-1} and 248 nm·cm^{-1}, while B should be close to 0 cm^{-1}.[8, 9] These extreme limits correspond to Models 1 and 3 in Table S1.

Another model for the diameter dependence is described by $\omega_{RBM} = (227/d_t)\sqrt{1 + C_e \cdot d_t^2}$, where C_e is a constant sensitive to the environment surrounding the nanotubes.[4, 10] If peaks *g*, *h*, and *i* are assigned to (8,4), (9,2), and (6,5),[11]

we obtain $C_e = 0.046\ nm^{-2} \pm 0.020\ nm^{-2}$, which corresponds to Model 2 in Table S1. This model likely corresponds to the most likely peak assignment.

		Extreme Case 1		Most Likely Assignment		Extreme Case 2	
Peak Label (Fig 3)	Raman Shift (cm^{-1})	Diameter (nm) Model 1 A = 227 $nm \cdot cm^{-1}$, B = 0 cm^{-1}	Assignment Model 1 A = 227 $nm \cdot cm^{-1}$, B = 0 cm^{-1}	Diameter (nm) Model 2 $C_e = 0.046$ nm^{-2}	Assignment Model 2 $C_e = 0.046$ nm^{-2}	Diameter (nm) Model 3 A = 248 $nm \cdot cm^{-1}$, B = 0 cm^{-1}	Assignment Model 3 A = 248 $nm \cdot cm^{-1}$, B = 0 cm^{-1}
a	145	1.57	S	1.66	S	1.71	S
b	177	1.28	S (E_{33}^S) or M (E_{11}^M)	1.33	S (E_{33}^S) or M (E_{11}^M)	1.40	S (E_{33}^S) or M (E_{11}^M)
c	192	1.18	S (E_{33}^S) or M (E_{11}^M)	1.22	S (E_{33}^S) or M (E_{11}^M)	1.29	S (E_{33}^S) or M (E_{11}^M)
d	217	1.05	M (E_{11}^M)	1.07	M (E_{11}^M)	1.14	M (E_{11}^M)
e	230	0.99	M (E_{11}^M)	1.01	M (E_{11}^M)	1.08	M (E_{11}^M)
f	236	0.96	M (E_{11}^M)	0.98	M (E_{11}^M)	1.05	M (E_{11}^M)
g	273	0.83	(8, 4) S (E_{22}^S)	0.85	(8, 4) S (E_{22}^S)	0.91	(11,1) S (E_{22}^S)
h	290	0.78	(9,2) S (E_{22}^S)	0.79	(9,2) S (E_{22}^S)	0.86	(8, 4) S (E_{22}^S)
i	307	0.74	(6,5) S (E_{22}^S)	0.75	(6,5) S (E_{22}^S)	0.81	(9,2) S (E_{22}^S)

S=semiconducting, M=metallic

Table S1. Radial Breathing Mode assignments

Assignments using these three models are graphically shown in Figures S1 to S3. Assignments from Models 1 and 2 are probably more accurate than those in Model 3.

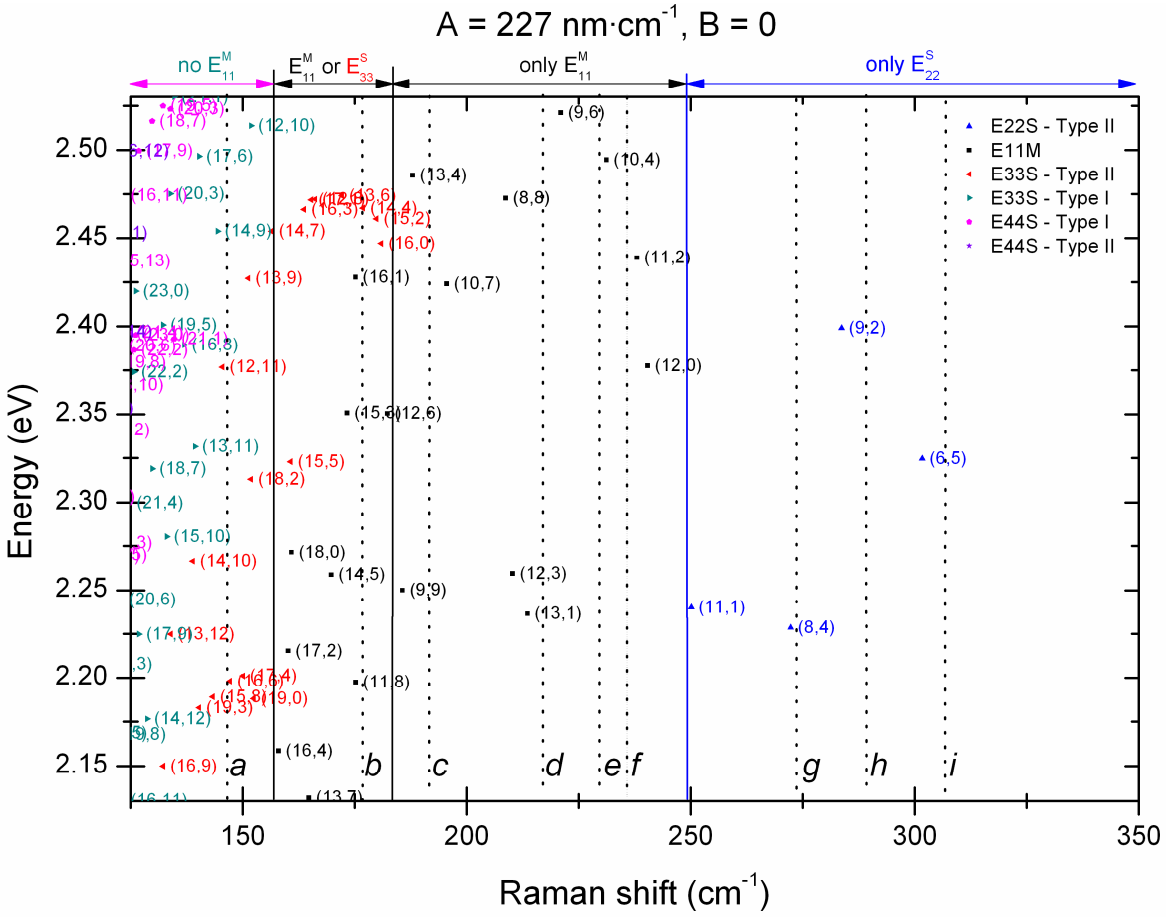

Figure S1. Kataura plot for the Extreme Case of Model 1. Frequencies were calculated using the expression $\omega_{RBM} = A/d_t + B$, where A = 227 nm·cm^{-1}, B = 0 cm^{-1}. Different (n,m) values are present. Only diameters larger than 0.7 nm are shown. Dotted lines represent observed RBMs shown in Figure 3. Points are labelled by the band they originate in. Semiconducting, metallic and mixed regions are delineated with respect to

the labels along the top axis, indicating the band of origin (e.g. E_{11}^{M} is metallic, E_{22}^{S} is semiconducting) along the top horizontal axis.

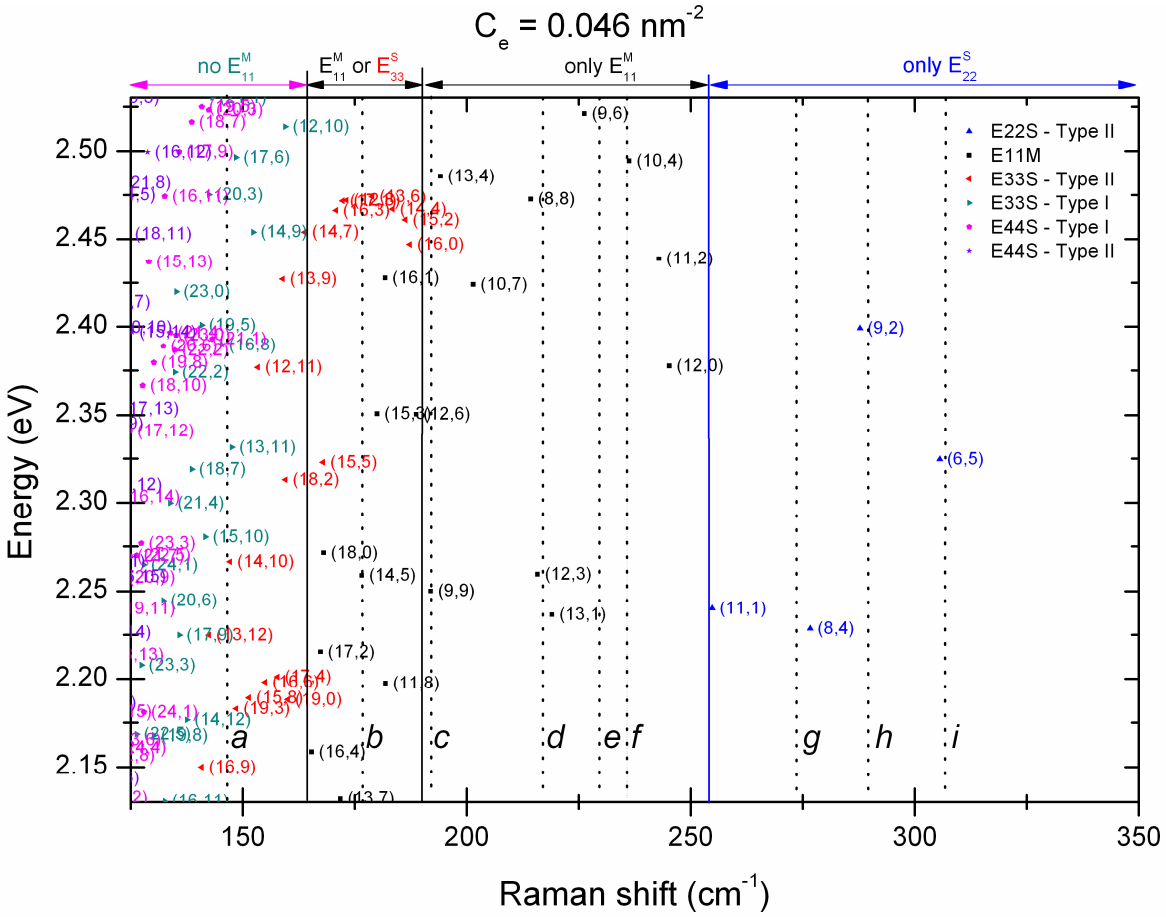

Figure S2. Kataura plot for the Most Likely Assigment of Model 2. Frequencies were calculated using the expression $\omega_{RBM} = (227/d_t)\sqrt{1 + C_e \cdot d_t^2}$, where $C_e = 0.046$ nm^{-2}. Different (n,m) values are present. Only diameters larger than 0.7 nm are shown. Dotted lines represent observed RBMs shown in Figure 3. Points are labelled by the band they originate in. Semiconducting, metallic and mixed regions are delineated with respect to the labels along the top axis, indicating the band of origin along the top horizontal axis.

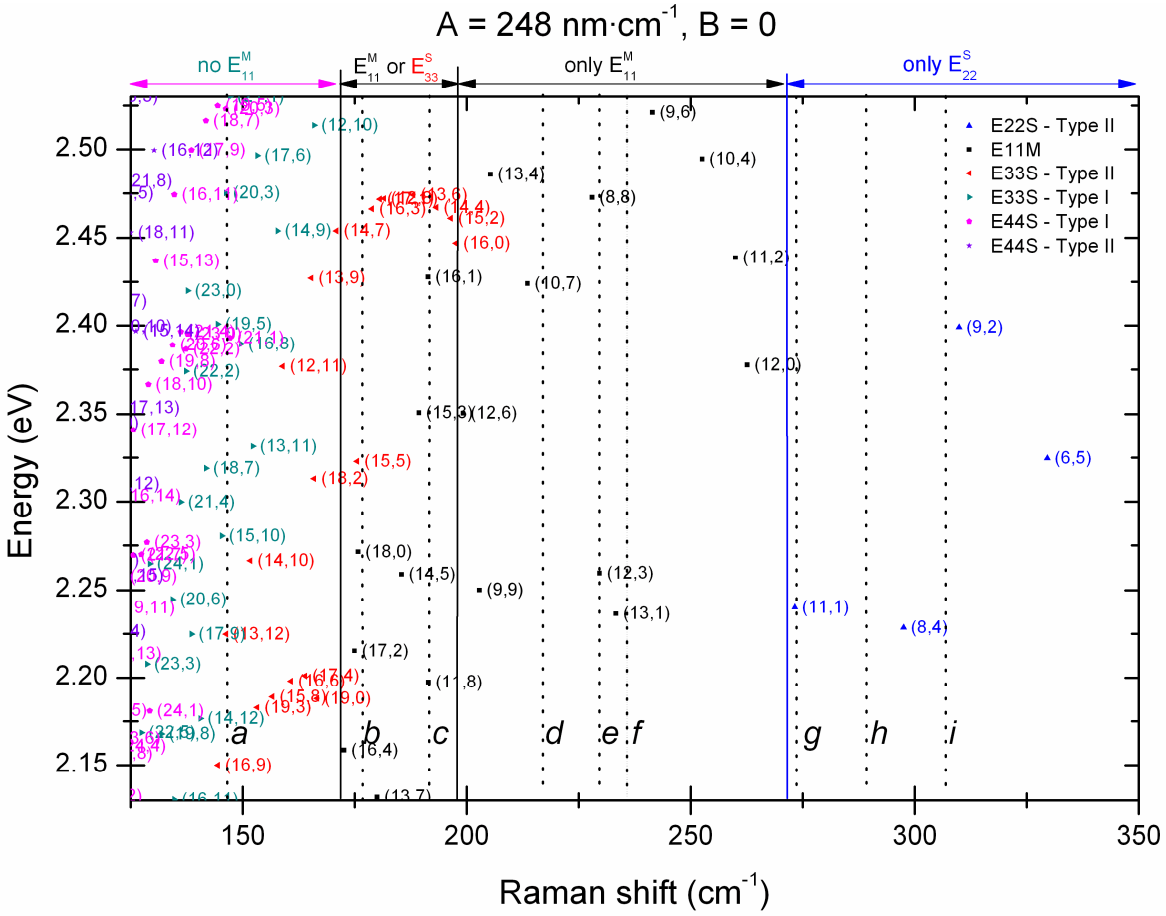

Figure S3. Kataura plot for the Extreme Case of Model 3. Frequencies were calculated using the expression $\omega_{RBM} = A/d_t + B$, where A = 248 nm·cm^{-1}, B = 0 cm^{-1}. Different (n,m) values are present. Only diameters larger than 0.7 nm are shown. Dotted lines represent observed RBMs shown in Figure 3. Points are labelled by the band they originate in. Semiconducting, metallic and mixed regions are delineated with respect to the labels along the top axis, indicating the band of origin along the top horizontal axis.

There is no obvious scaling of etch rates with chiral angle. However, all three models predict that peak *a* is semiconducting (E_{33}^S or E_{44}^S), peaks *d* to *f* are metallic

(E_{11}^M), and peaks *g* to *i* are semiconducting (E_{22}^S). Peaks *b* and *c* may be either type (E_{11}^M or E_{22}^S).

We can similarly use the G- peaks in Figure 3 for assignment; see Table S2.[3, 9] The G- resonance window is larger than the RBM resonance window. As a result, while all the strongest RBM peaks should produce visible G- peaks, some G- peaks may correspond to RBMs that are off-resonance and not visible. The center of the windows and window width may shift depending whether the plot corresponds well to sample environment. For example, CNT bundling can widen the RBM window.[6, 12]

Label	Raman Shift (cm^{-1})	Diameter (nm)	Assignment	Comments
I	~1504 cm^{-1}	~0.85	M	Corresponds to unresolved RBMs at 240-255 cm^{-1}
II	1523 cm^{-1}	0.75 (1.00)	S (M)	Corresponds to RBM-*i* (overlapping RBM-*d* to *f*)
III	1540 cm^{-1}	~0.85	S	Corresponds to RBM-*g* or *h*
IV	~1562 cm^{-1}	~1.20	S	Corresponds to RBM-*b* and/or RBM-*c*
V	1570 cm^{-1}	~1.50	S	Corresponds to RBM-*a*

Table S2. G- band assignments

The (6,5) nanotube, assigned to peak-*i* in Model 1, is highly resonant and was found by Telg et al. to generate a G- at 1528 cm^{-1}.[3] This likely corresponds to the G- peak near 1523 cm^{-1} (peak-II). Also in this spectral range are metallic peaks from larger diameter nanotubes. Although the (6,4) species may also contribute, it is not clearly visible in the RBM region.

If the 1540 cm^{-1} peak is semiconducting it should correspond to diameters of close to ~0.85 nm.[3, 9] For Model 1 this would correspond to ~270 cm^{-1} (peak-*g*), or for Model 3 this would correspond to 290 ~cm^{-1} (peak-*h*). In either assignment these peaks are semiconducting.

The low intensity G- peak at ~1504 cm^{-1} is most likely to be metallic. A semiconducting nanotube in this would not be very stable as it would correspond to diameters of ~0.5 nm. Additionally, the lineshape of the G- in this region appears to be asymmetric, likely having a "Breit-Wigner-Fano lineshape" typical of metallic CNTs. Metallic tubes with this resonance are ~1 nm in diameter, and thus this correlates well with the large unresolved RBM shoulder at around 240-250 cm^{-1}.

After the etching procedure all the previously discussed G- peaks are destroyed. However, as shown in Figure 3(a), RBMs-*b* and *c* (i.e. 177 cm^{-1} and 192 cm^{-1}) are fairly persistent. Notably, the G- doublet (i.e. 1562 cm^{-1} and 1570 cm^{-1}) in Figure 3(b) is also persistent. The presence of a semiconducting G- near 1562 cm^{-1} suggests that at least one of *b* and *c* are semiconducting, if not both. The peak at 1570 cm^{-1} likely corresponds to the semiconducting RBM-*a*.[3]

2. Raman spectra of sample etched at T = 600°C

The result of etching at T = 600 °C is presented in Figure S4. As seen in Figure 2(a), the ~10 RBMs of interest at low temperature are also present at high temperature, although individual RBM peaks have downshifted, and not all the same RBM peaks are visible due to the change in resonance conditions. We indicate peaks *a*: 140 cm^{-1}, *b*: 168 cm^{-1}, c: 185 cm^{-1}, *d:* 203 cm^{-1}, *d**: 211 cm^{-1}, *e*: 225 cm^{-1}, *f*: 240 cm^{-1}, *g*: 260 cm^{-1}, *g**: 266 cm^{-1}, *h*: 280 cm^{-1}, *i*: 290 cm^{-1}. RBMs-*d*/*d** and *g*/*g** may be doublet peaks, perhaps containing peaks from species only resonant at high temperatures. A 295 cm^{-1} SiO_2 background peak (blue) is present.

RBM etching is much more complete than in the low temperature case and air input was stopped (at t = 16 min) before the sample was entirely etched away. It appears that the diameter dependence is more pronounced at these high temperatures, or alternatively, when the etching is continued for a long time. Similar trends are likely present but less pronounced than at low temperatures. For example, it is unclear whether the higher etching temperature reduces etching peak-*c* selectivity, although the spectrum at t = 3 min 30 s seems comparable to the final spectrum in Figure 2a. The weak RBM-*a* peak is difficult to track visually, but seems to vanish the earliest after t = 2 min 30 s.

The corresponding change in the normalized G and D bands is much more pronounced in Figure 3(b) and 3(c), respectively. After t = 9 min 30 s, the G band is still easily visible, though much sharper, and the D band has completely vanished. Prior to this, the D band frequency upshifts from 1316 cm^{-1} to 1323 cm^{-1}, indicating a change in bundling or a loss in resonant small diameter nanotubes.[5] Likewise, the loss in G-

intensity below 1567 cm^{-1} is much more significant than for the lower etch temperature case. The loss in Breit-Wigner-Fano (BWF) character in the G- region is obvious, suggesting that the surviving RBM-c and RBM-d peaks correspond, at least in part, to semiconducting species.

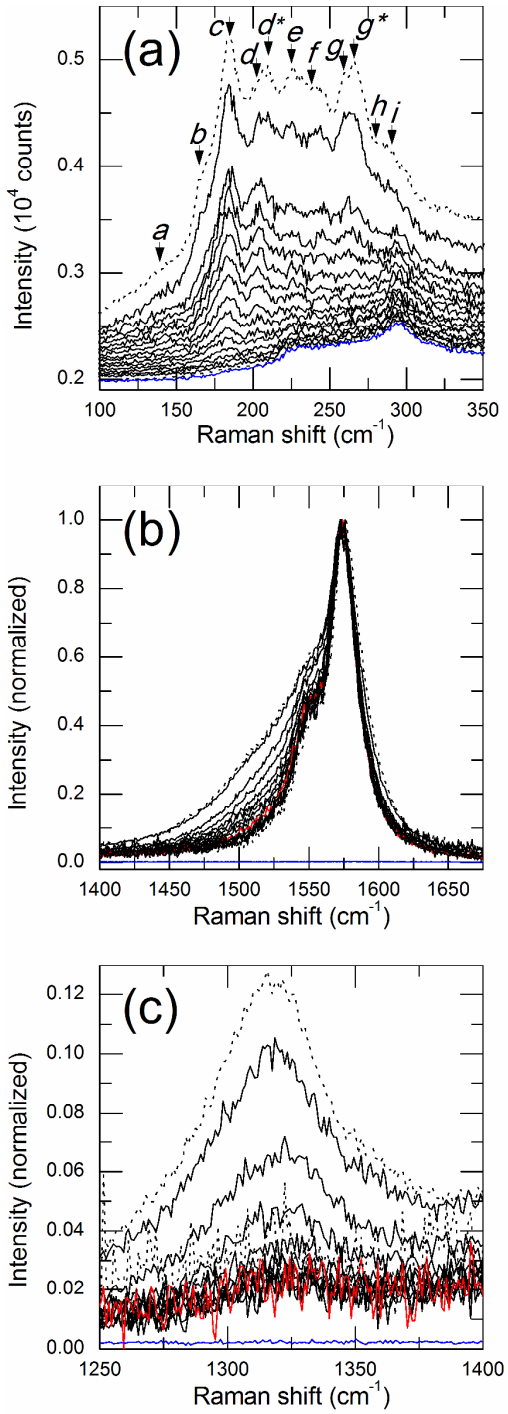

Figure S4. *In situ* Raman spectra of a sample being etched at 600 °C, displayed chronologically from top to bottom. (a) Spectral changes in the RBM region. Also shown are corresponding changes to (b) G and (c) D bands. The top and bottom dotted spectra

correspond respectively to pre- and post-etch spectra (after t = 16 min) for the sample (30 s exposure and scaled to black frames). The correspond Si/SiO_2 backgrounds are displayed in blue. In (a) the spectra are shown every 1 min, from t = 30 s to t = 14 min 30 s, with air input occurring at t = 0 s. In (b) and (c), every spectrum is normalized to their maximum G band intensity. In (b), spectra are shown every 1 min, from t = 30 s to t = 12 min 30 s. In (c), spectra are shown every 1 min, from t = 30 s to t = 10 min 30 s.

3. RBM Time Evolution Curves

Figure S5 displays the time evolution of the most intense RBM peaks for the 350°C air etched sample, compared with the time evolution of the G and D bands. With respect to the peaks in Figure 2(a), the evolution of peaks-*b*, *c*, and *g* are plotted. The evolution of peaks-*e* and *f* is also plotted, but since the peaks overlap, the sum of both signals was plotted together. As usual, peak evolution is scaled with respect to the Si band, and normalized with respect to peak signal at t = 0 s.

A significant amount of noise is present in these curves due to the comparatively low signals of the RBM peaks. Data extraction is further complicated by the presence of a non-flat background and unresolved RBMs that are close to the distinct RBM peaks.

The RBM time evolution curves correspond well with the changes directly observed in Figure 2(a). RBM-*c* is by far the most persistent peak followed by RBM-*g*. The likely E_{11}^{M} peaks at *e* and *f* etch rapidly. The RBM-*b* shoulder peak also appears to decrease very rapidly, however it must be noted that as a shoulder peak, background subtraction is particularly subject to error. A simple model with an increasing etch rate with decreasing diameter cannot explain the extracted RBM evolution curves as we have in order of etch rate b>e+f>g(>D>G>)c where if the order were determined by this simple model we would have g>e+f>c>b which is not observed.

As shown in Figure 5, the G band tracks relatively well with the persistent RBM-*c* peak. This makes some sense since CNTs corresponding to the other RBMs are destroyed and cannot contribute as much to the G band.

Another simple model might be that the etch rate is determined by sidewall defects, with tubes etching proportionally with their defect densities. In that case one would expect an etch rate proportional to the D band intensity. With the exception of perhaps the RBM-*g* this is not the case, and such a defect etching model can be ruled out.

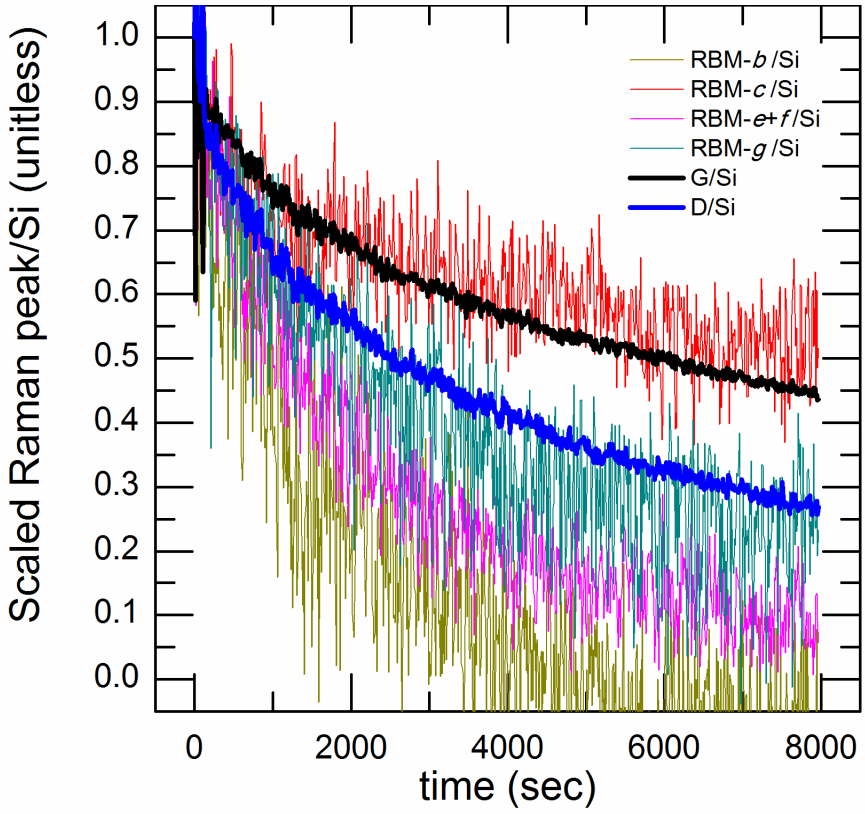

Figure S5. Time evolution of Raman peaks compared with the G and D bands for the sample etched at 350°C. The evolution curves of the scaled, normalized peaks at 177 cm^{-1} (dark yellow), 192 cm^{-1} (red), 230 cm^{-1} and 236 cm^{-1} (magenta), 273 cm^{-1} (dark cyan), alongside the G (black) and D bands (blue), are plotted.

4. D/G Time Evolution Curves

Figure S6 displays the D/G time evolution for all samples from T = 300 °C to 600 °C. The 500 °C sample was more crystalline to begin with and therefore has the least signal due its low D band values. Also note that at higher etch temperatures, pre-etch D band intensities were lowered more than the pre-etch G band intensities due to the change in resonance, so the initial D/G values scale with temperature to an extent. Comparing these values to Figure 4, one can show that D/G time evolution scales directly with remaining G band intensity independently of etching temperature, at least for low temperatures. For example, from T = 350 °C to 500 °C the D/G ratio drops by ~33%, once G band intensity falls by 50%. To obtain high crystallinity samples, prolonged etching is required. For a ~80% drop in D/G, the G band intensity must fall by 72%, and for a ~90% drop in D/G, G band intensity must fall by 80%.

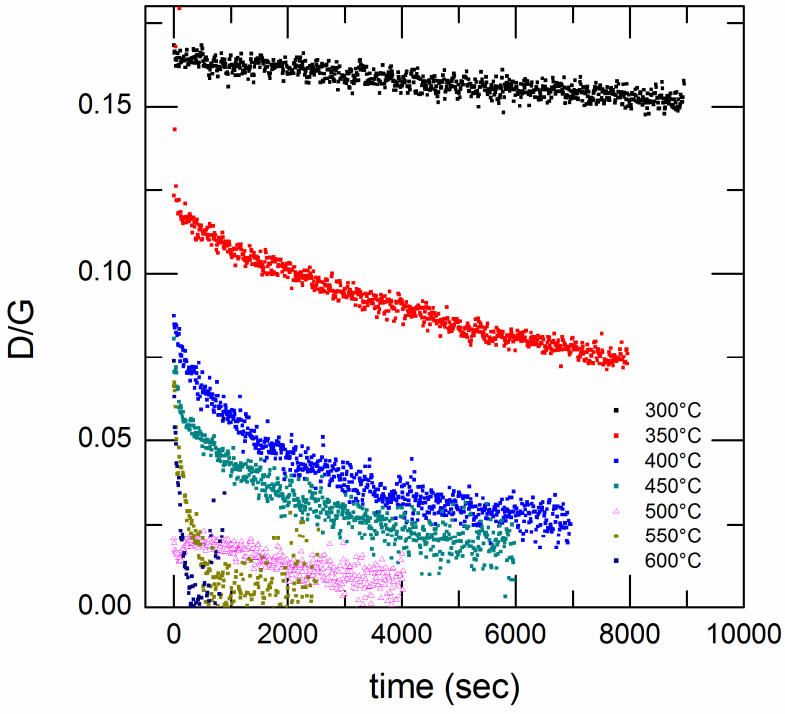

Figure S6. D/G time evolution normalized to initial values from T = 300 °C to 600 °C.

5. Alternative Activated Plots

Instead of performing the biexponential fit shown in Figure 5, one exponential can be fit at early times (red) and one exponential can be fit at late times (green) as shown in Figure S7. These fits were performed for all G and D band time evolution curves, such that time constants τ_{fast} and τ_{slow} can be obtained from the fast (red) and slow (green) components, as they were for the biexponential fit.

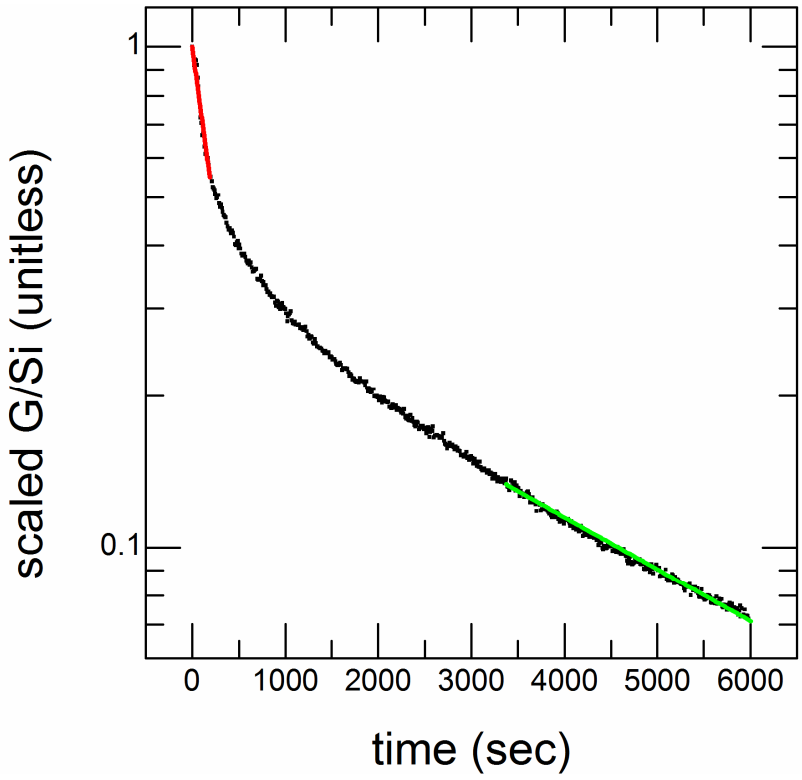

Figure S7. Alternative two exponential fit of the G band signal (normalized to the Si intensity) for the 450° C etched sample. Independent slow (green) and fast (red) fits are indicated.

Using this alternative fitting scheme, alternative activation plots for the G and D bands are given in Figure S8. The fast (black squares) and slow (red squares) G band etch rates are activated with energies 0.53 eV ± 0.10 eV and 0.47 eV ± 0.07 eV, respectively. The fast (blue triangles) and slow (green triangles) D band etch rates are activated with energies 0.63 eV ± 0.11 eV and 0.39 eV ± 0.07 eV, respectively. The large uncertainty makes these activation energies barely distinguishable if at all.

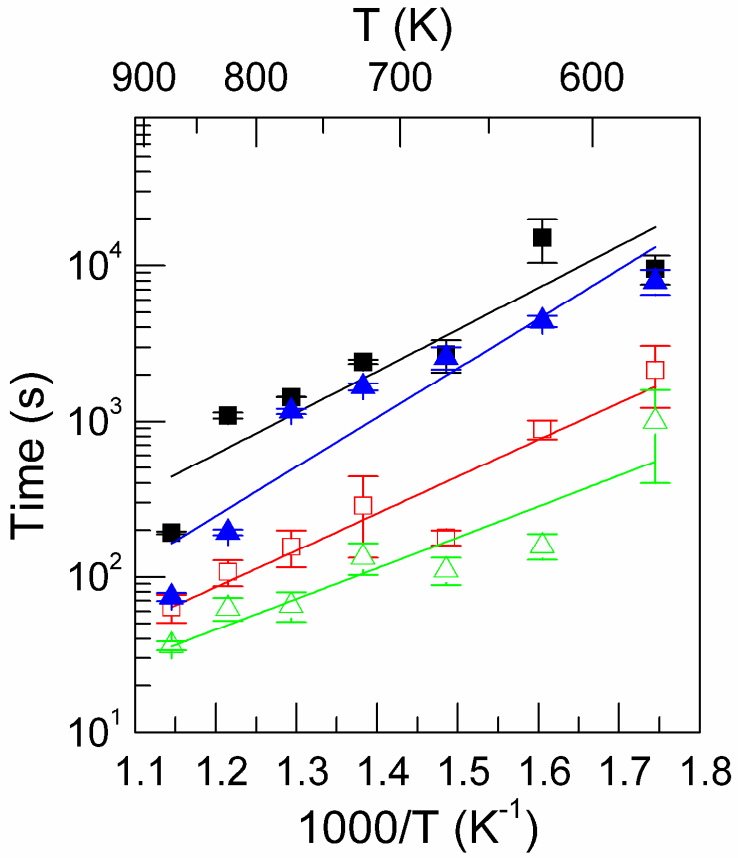

Figure S8. Activation plots for the G band fast (black square) and slow (red square) τ values and for the D band fast (blue triangle) and slow (green triangle) τ values. Activation energies are taken from the slopes of the four linear fits and are listed above.

6. TEM images

Transmission electron microscope (TEM) images of a typical pre-etch sample, taken using a JEOL JEM-2100F TEM, are shown in Figure S9. CNTs were transferred by mechanically passing the surface of the sample across a carbon TEM grid.

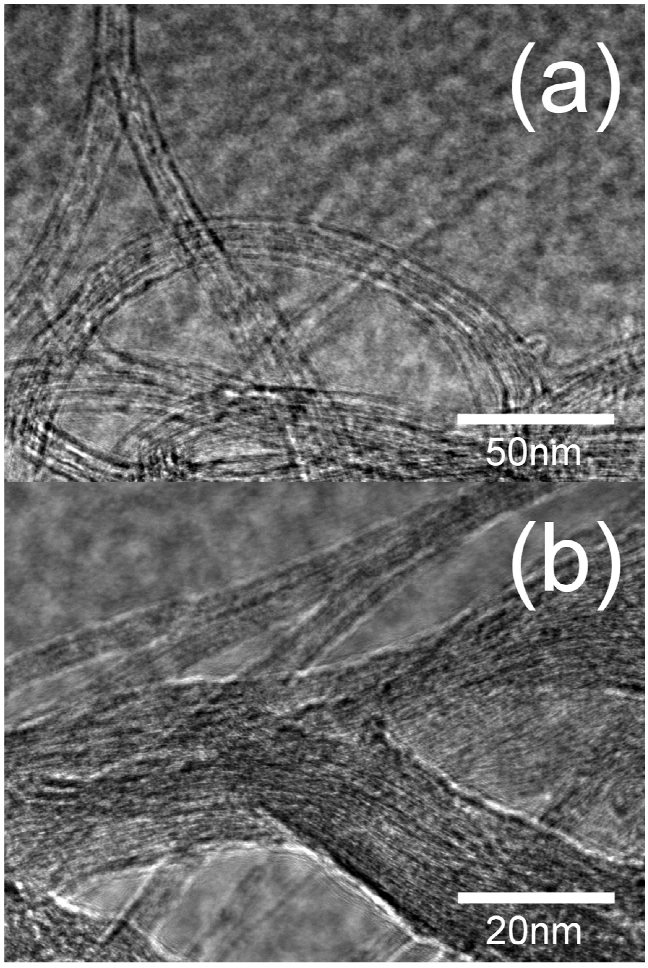

Figure S9. Typical TEM micrographs of the pre-etch sample at different magnifications.

As seen in Figure S9, SWNT bundles <25 nm in thickness are typical, such that thicker bundles often split into thinner bundles and individual SWNTs. Individual CNTs with diameters <5 nm and thin bundles composed of 2-3 CNTs are visible. We were able

to find some isolated individual nanotubes, but they degraded quickly in the TEM. Most tubes were bundled however, and these were more stable in the beam.

From the TEM images we note that large isolated pieces of amorphous carbon are not visible. However, there may be unresolved graphitic carbon coatings intimately contacting the surfaces of nanotubes or bundles. We lack the TEM resolution here to distinguish them. The CNT walls do not appear to be particularly defective.

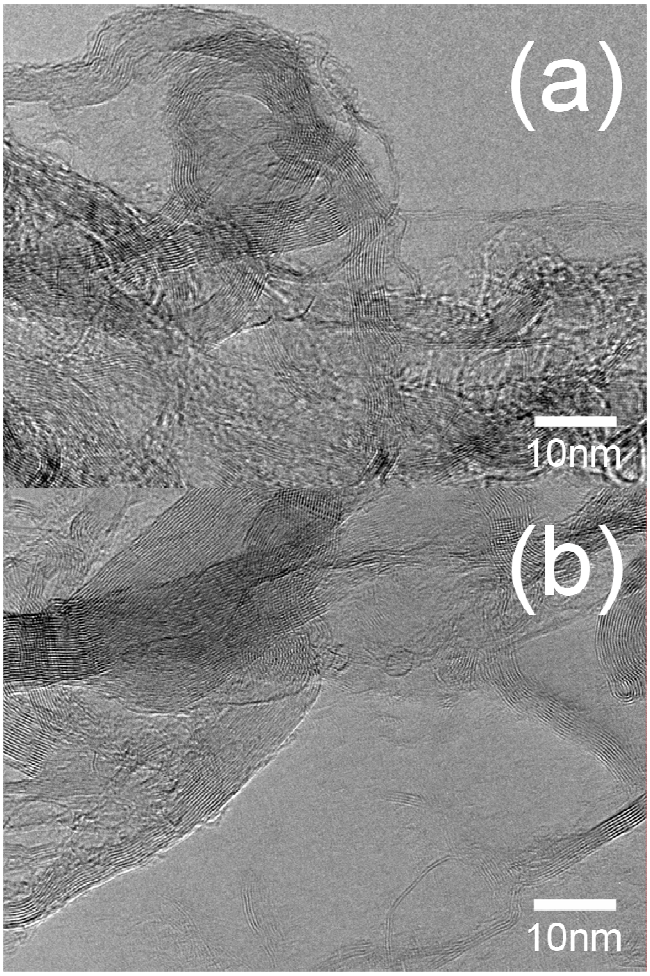

Figure S10: High resolution TEM micrographs of the pre-etch sample.

High-resolution TEM (HRTEM) images of the pre-etch sample were also taken using a Titan^3 80-300 TEM operated at 300 keV. CNTs were transferred by mechanically rubbing the nanotube sample surface onto a lacey carbon grid. Two typical images (a) and (b) are shown in Figure S10.

Consistent with the SEM observations and Raman data, the vast majority nanotubes are organized into bundles, ranging here from ~2 nm to ~10 nm in width. These bundles are extremely well graphitized, with little if any evidence of any amorphous carbon in their interiors. They can be seen to cross in front of other bundles and bundle together into networks in many cases. Individual SWNTs of different diameters can also be seen in places. For the most part the individual nanotubes and bundles of nanotubes appear largely free of coatings, despite the fact that we were looking for examples of particularly coated nanotubes. In some places in these images it is possible to see what might be thin layers of poorly structured carbon on the outside of bundles or individual nanotubes. However, image artifacts such as those due to depth of focus and motion make this unclear, and furthermore TEM induced damage and deposition may also contribute. Certainly, as in the low resolution TEM, there is no evidence of large flakes of amorphous carbon. Here many clean nanotubes and bundles of nanotubes are seen. The level of non-nanotube carbon coating thus appears quite limited, consistent with the XPS, SEM and Raman data.

7. *Ex situ* Raman spectral changes to 400°C etched sample with four laser lines

The *ex situ* Raman spectra of the CNT sample etched at 400°C was obtained using four laser excitation wavelengths at 514 nm, 532 nm, 633 nm, and 785 nm. Both the pre- and post-etch Raman spectra were collected at room temperature for each laser line. The *ex situ* 532 nm spectra were taken using the same apparatus and setup as all the *in situ* spectra. The 514 nm, 633 nm, and 785 nm spectra were taken using a commercial Renishaw inVia Raman microscope system using a slit illuminated 20× objective, with incident laser powers <1 mW. The 532 nm spectra were taken on the same sample and location before and after etching, while the remaining spectra were taken on separate samples and different locations.

These spectra are presented in Figure S11. Spectra above 1692 cm^{-1} for the 532 nm spectra could not be collected. Pre- and post-etch signal intensities were normalized by setting the spectral baseline to 0 and the height of the first order Si band at 520 cm^{-1} to 1. The post-etch spectra were also scaled (blue line) so that the G band maxima and neighboring baselines matched those of the pre-etch spectra. The 2D band profile for the 532 nm spectra was not obtained.

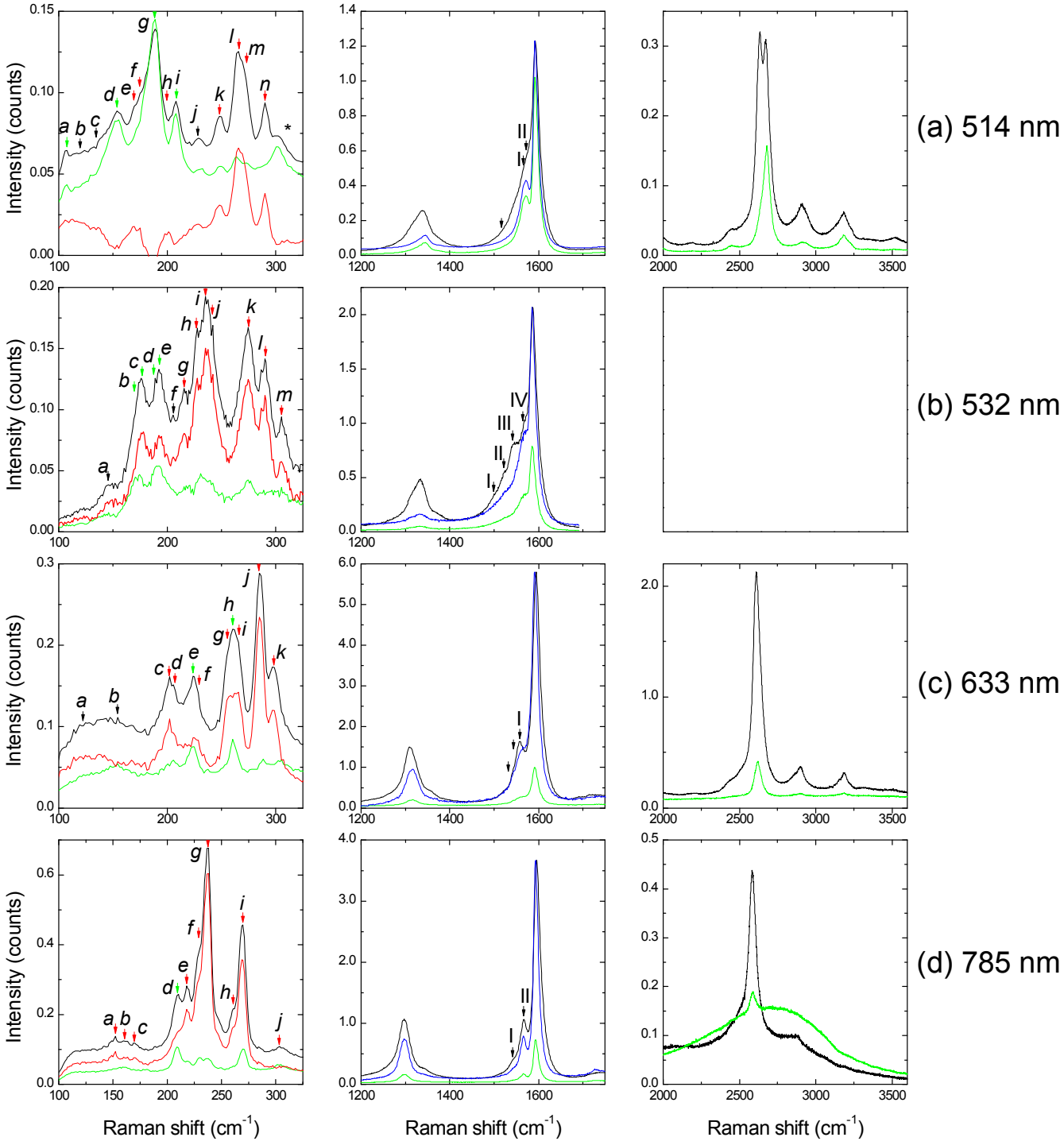

Figure S11. *Ex situ* Raman spectra of pre- (black) and post-etched (green) sample performed with (a) 514 nm, (b) 532 nm, (c) 633 nm, and (d) 785 nm laser lines. The sample was etched at 400°C. Spectra above 1692 cm^{-1} were not collected using the 532 nm laser line. The difference between the pre- and

post-etch spectra is shown in red. Blue spectra shows the scaled post-etch spectra (see text). Asterisks indicate peaks originating from Si/SiO_2.

As we shall describe, these spectra show the rapid etching of E_{11}^M, E_{11}^S, E_{22}^S nanotubes versus comparatively resistant E_{33}^S and E_{44}^S nanotubes in way that cannot be solely explained by diameter dependence. In Table S3, the labelled RBM peaks in Figure S11 are chirality/type assigned using the Models described in Section 1 of the SI. Likewise G- assignment is tabulated in Table S4. Sample Kataura plots using $C_e = 0.046$ nm^{-2} are shown for each of the four laser lines in Figures S12-S15. Again, Kataura plots are obtained using data from R. Saito's Exciton Kataura Plot page (i.e. http://flex.phys.tohoku.ac.jp/eii/).[1, 2] Individual RBMs were indicated as being resistant (green arrow, dotted line) or non-resistant (red arrow, dotted line) to etching based on the relative intensity change before and after etching.

For the 514 nm spectra, the high intensity *d*, *g*, and *i* peaks have undergone little or no etching when compared to the almost totally etched peaks *k* to *n*. However, the low intensity *b*, *c*, *e*, *f*, and *h* peaks also etch faster than the *d*,*g*, and *i* peaks despite their varying diameters. From the Kataura plot we see that the transition between metallic E_{11}^M and semiconducting E_{22}^S species occurs starting at peaks *h* or *g*. Therefore, despite probably being a E_{11}^M nanotube, peak *i* surprisingly etches slowly. One possible assignment for this peak is the high chiral angle (8,8) nanotube, but this is again surprising since higher chiral angle nanotubes are expected to etch more rapidly.[13, 14]

The pre-etch G band of the 514 nm spectra contains unresolved G- peaks between 1500-1540 cm^{-1}, probably containing contributions from the resonant E_{11}^M species. RBM peaks l and m are expected to contribute peaks close to 1540-1550 cm^{-1}, although these peaks are not distinctly visible.

The two most intense G- that persist after etching are peaks II and its shoulder peak I; these correspond nicely with the resistive RBMs at peaks *d* and *g*.

After etching, the D band upshifts from 1338 cm^{-1} to 1344 cm^{-1}, perhaps indicating a minor change in the amount of bundling in the sample or in defective carbon after etching. Notably the 2D peak changes from two peaks centered at 2635 cm^{-1} and 2670 cm^{-1}, to one peak at 2679 cm^{-1}. Different species of SWNT have different 2D peak structures, including doublets.[15] The change in 2D from doublet to single peak may originate in the change in tube distribution.

The 532 nm spectra is similar to previously shown *in situ* data. The RBMs labelled *b* to *e* are resistant compared to the other peaks, while corresponding with the onset of E_{33}^{S} nanotubes in the Kataura plot. The metallic RBMs at peaks *g* to *j* etch as much as the smaller diameter E_{22}^{S} species *k* to *m*. The low intensity RBM-*a* also appears to etch despite being of large diameter, while peak *c* appears to etch slightly more than the smaller diameter peak *e*.

Poorly resolved G- peaks close to peak I should be generated with metallic RBMs such as RBMs *i* and *j*. Likewise peak II can be attributed to metal peaks close to RBM-*g*. The other indicated G-peaks III and IV correspond to the E_{22}^{S} and E_{33}^{S} peaks respectively. This assignment makes sense, since the peak IV appears far more resistant than peak III, and the larger diameter E_{33}^{S} peaks are generally more resistant than the E_{22}^{S} peaks.

The D band at 1333 cm^{-1} does not shift following etching.

The 633 nm RBMs are fairly unstable, with the two most comparatively resistant RBMs being peaks *e* and *h*, which are semiconductors. All the labelled peaks after (and including) peak *e* appear to correspond to small diameter E_{22}^{S}, with peaks *b* to *c* being likely metallics. Large diameter semiconducting peaks before 150 cm^{-1} are not clearly visible. We see that the larger diameter peak *c, a*

metallic tube, does etch faster than peak *e*, a semiconductor, consistent again with the idea that nanotube type may directly affect etching rate. Peak *h* is flanked by two nanotubes of similar diameter that etch more than peak *h* itself indicating indicated a strong chiral dependence on etching rates for these tubes even though they are the both semiconductors.

There are again unresolved low frequency G- peaks present, such that we expect RMBs *c*, *j* and *h* to have G- peaks close to 1532 cm^{-1}, 1543 cm^{-1} and 1548 cm^{-1}. The somewhat resistant peak I corresponds well with the somewhat resistant RBM *e*.

The associated D band experiences a 5 cm^{-1} upshift from 1310 cm^{-1} after etching, while the 2D experiences a comparable shift from 2610 cm^{-1} to 2621 cm^{-1}.

The 785 nm RBMs also experience significant loss, with peaks *i* and *j* corresponding to E_{11}^{S} species, peaks *d* to *h* being E_{22}^{S} nanotubes, with peaks *a* to *c* being either E_{22}^{S} or E_{11}^{M}. The most resistant peak is RBM *d*, a semiconductor. The small diameter RBM *i* appears to be somewhat more resistant than peak *g*, possibly because peak *i* probably corresponds to a low chiral angle species.

In terms of the G- peaks, peak *g* should match with a G- at 1555 cm^{-1}, while peak *i* should have a peak at 1547 cm^{-1} (perhaps corresponding to peak I), both of which may be present as weak peaks in the pre-etch sample. The persistent semiconducting peak II corresponds well with RBM *d*, as expected.

Neither the D band at 1298 cm^{-1} or the 2D band at 2584 cm^{-1} experience major shifts to frequency or lineshape following etching. The broad hill between 2000-3250 cm^{-1} is attributed to the sample background.

Table S3a. Radial Breathing Mode assignments for E_{LASER} = 514 nm (2.41 eV)

		Extreme Case 1		Most Likely Assignment		Extreme Case 2	
Peak Label	Raman Shift (cm^{-1})	Diameter (nm) Model 1 A = 227 $nm \cdot cm^{-1}$, B = 0 cm^{-1}	Assignment Model 1 A = 227 $nm \cdot cm^{-1}$, B = 0 cm^{-1}	Diameter (nm) Model 2 C_e = 0.046 nm^{-2}	Assignment Model 2 C_e = 0.046 nm^{-2}	Diameter (nm) Model 3 A = 248 $nm \cdot cm^{-1}$, B = 0 cm^{-1}	Assignment Model 3 A = 248 $nm \cdot cm^{-1}$, B = 0 cm^{-1}
a	107	2.12	S	2.38	S	2.32	S
b	120	1.89	S	2.07	S	2.07	S
c	134	1.69	S	1.82	S	1.85	S
d	154	1.47	S	1.55	S	1.61	S
e	170	1.34	S (E_{33}^S) or M (E_{11}^M)	1.39	S (E_{33}^S) or M (E_{11}^M)	1.46	S
f	174	1.30	S (E_{33}^S) or M (E_{11}^M)	1.36	S (E_{33}^S) or M (E_{11}^M)	1.43	S (E_{33}^S) or M (E_{11}^M)
g	189	1.20	M (E_{11}^M)	1.24	S (E_{33}^S) or M (E_{11}^M)	1.31	S (E_{33}^S) or M (E_{11}^M)
h	200	1.14	M (E_{11}^M)	1.17	M (E_{11}^M)	1.24	S (E_{33}^S) or M (E_{11}^M)
i	208	1.09	M (E_{11}^M)	1.12	M (E_{11}^M)	1.19	M (E_{11}^M)
j	227	1.00	M (E_{11}^M)	1.02	M (E_{11}^M)	1.09	M (E_{11}^M)
k	248	0.92	S (E_{22}^S) or M (E_{11}^M)	0.93	M (E_{11}^M)	1.00	M (E_{11}^M)
l	266	0.85	S (E_{22}^S) or M (E_{11}^M)	0.87	S (E_{22}^S) or M (E_{11}^M)	0.93	M (E_{11}^M)
m	270	0.84	S (E_{22}^S) or M (E_{11}^M)	0.85	S (E_{22}^S) or M (E_{11}^M)	0.92	S (E_{22}^S) or M (E_{11}^M)
n	290	0.78	(9,2), (6,5) ? S (E_{22}^S)	0.79	(9,2) S (E_{22}^S)	0.86	S (E_{22}^S) or M (E_{11}^M)

Table S3b. Radial Breathing Mode assignments for E_{LASER} = 532 nm (2.33 eV)

			Extreme Case 1		Most Likely Assignment		Extreme Case 2	
Peak Label (Fig S10b)	Corres-ponding Peak Label used in Fig 3	Raman Shift (cm^{-1})	Diameter (nm) Model 1 A = 227 $nm \cdot cm^{-1}$, B = 0 cm^{-1}	Assignment Model 1 A = 227 $nm \cdot cm^{-1}$, B = 0 cm^{-1}	Diameter (nm) Model 2 C_e = 0.046 nm^{-2}	Assignment Model 2 C_e = 0.046 nm^{-2}	Diameter (nm) Model 3 A = 248 $nm \cdot cm^{-1}$, B = 0 cm^{-1}	Assignment Model 3 A = 248 $nm \cdot cm^{-1}$, B = 0 cm^{-1}
a	*a*	146	1.55	S	1.65	S	1.70	S
b	-	170	1.34	S (E_{33}^S) or M (E_{11}^M)	1.39	S (E_{33}^S) or M (E_{11}^M)	1.46	S
c	*b*	177	1.28	S (E_{33}^S) or M (E_{11}^M)	1.33	S (E_{33}^S) or M (E_{11}^M)	1.40	S (E_{33}^S) or M (E_{11}^M)
d	-	189	1.20	S (E_{33}^S) or M (E_{11}^M)	1.24	S (E_{33}^S) or M (E_{11}^M)	1.31	S (E_{33}^S) or M (E_{11}^M)
e	*c*	193	1.18	S (E_{33}^S) or M (E_{11}^M)	1.22	S (E_{33}^S) or M (E_{11}^M)	1.28	S (E_{33}^S) or M (E_{11}^M)
f	-	205	1.11	(10,7) M (E_{11}^M)	1.14	(10,7) M (E_{11}^M)	1.21	(9,9) M (E_{11}^M)
g	*d*	215	1.06	(8,8) or (12,3) M (E_{11}^M)	1.08	(8,8) or (12,3) M (E_{11}^M)	1.15	(10,7) M (E_{11}^M)
h	*e*	227	1.00	(9,6) M (E_{11}^M)	1.02	(9,6) M (E_{11}^M)	1.09	(8,8) or (12,3) M (E_{11}^M)
i	*f?*	236	0.96	(10,4) M (E_{11}^M)	0.98	(10,4) M (E_{11}^M)	1.05	(13,1) M (E_{11}^M)
j	*f?*	240	0.95	(11,2) M (E_{11}^M)	0.97	(11,2) M (E_{11}^M)	1.03	(9,6) M (E_{11}^M)
k	*g*	275	0.83	(8,4) S (E_{22}^S)	0.84	(8,4) S (E_{22}^S)	0.90	(11,1) S (E_{22}^S)
l	*h*	290	0.78	(9,2) S (E_{22}^S)	0.79	(9,2) S (E_{22}^S)	0.86	(8,4) S (E_{22}^S)
m	*i*	306	0.74	(6,5) S (E_{22}^S)	0.75	(6,5) S (E_{22}^S)	0.81	(9,2) S (E_{22}^S)

Table S3c. Radial Breathing Mode assignments for E_{LASER} = 633 nm (1.96 eV)

		Extreme Case 1		Most Likely Assignment		Extreme Case 2	
Peak Label	Raman Shift (cm^{-1})	Diameter (nm) Model 1 A = 227 $nm \cdot cm^{-1}$, B = 0 cm^{-1}	Assignment Model 1 A = 227 $nm \cdot cm^{-1}$, B = 0 cm^{-1}	Diameter (nm) Model 2 C_e = 0.046 nm^{-2}	Assignment Model 2 C_e = 0.046 nm^{-2}	Diameter (nm) Model 3 A = 248 $nm \cdot cm^{-1}$, B = 0 cm^{-1}	Assignment Model 3 A = 248 $nm \cdot cm^{-1}$, B = 0 cm^{-1}
a	121	1.88	S	2.05	S	2.05	S
b	154	1.47	S (E_{33}^S) or M (E_{11}^M)	1.55	S (E_{33}^S) or M (E_{11}^M)	1.61	S (E_{33}^S) or M (E_{11}^M)
c	202	1.12	M (E_{11}^M)	1.16	M (E_{11}^M)	1.23	M (E_{11}^M)
d	206	1.10	M (E_{11}^M)	1.13	M (E_{11}^M)	1.20	M (E_{11}^M)
e	224	1.01	S (E_{22}^S)	1.04	S (E_{22}^S)	1.11	M (E_{11}^M)
f	228	1.00	S (E_{22}^S)	1.02	S (E_{22}^S)	1.09	S (E_{22}^S) or M (E_{11}^M)
g	257	0.88	S (E_{22}^S)	0.90	S (E_{22}^S)	0.96	S (E_{22}^S)
h	260	0.87	S (E_{22}^S)	0.89	S (E_{22}^S)	0.95	S (E_{22}^S)
i	265	0.86	S (E_{22}^S)	0.87	S (E_{22}^S)	0.94	S (E_{22}^S)
j	285	0.80	(7,5) or (8,3) S (E_{22}^S)	0.81	(7,5) S (E_{22}^S)	0.87	S (E_{22}^S)
k	298	0.76	(8,3) or (9,1) S (E_{22}^S)	0.77	(8,3) S (E_{22}^S)	0.83	(7,5) S (E_{22}^S)

Table S3d. Radial Breathing Mode assignments for E_{LASER} = 785 nm (1.58 eV)

		Extreme Case 1		Most Likely Assignment		Extreme Case 2	
Peak Label	Raman Shift (cm^{-1})	Diameter (nm) Model 1 A = 227 $nm \cdot cm^{-1}$, B = 0 cm^{-1}	Assignment Model 1 A = 227 $nm \cdot cm^{-1}$, B = 0 cm^{-1}	Diameter (nm) Model 2 C_e = 0.046 nm^{-2}	Assignment Model 2 C_e = 0.046 nm^{-2}	Diameter (nm) Model 3 A = 248 $nm \cdot cm^{-1}$, B = 0 cm^{-1}	Assignment Model 3 A = 248 $nm \cdot cm^{-1}$, B = 0 cm^{-1}
a	152	1.49	S (E_{22}^S) or M (E_{11}^M)	1.58	S (E_{22}^S) or M (E_{11}^M)	1.63	S (E_{22}^S) or M (E_{11}^M)
b	159	1.43	S (E_{22}^S) or M (E_{11}^M)	1.50	S (E_{22}^S) or M (E_{11}^M)	1.56	S (E_{22}^S) or M (E_{11}^M)
c	170	1.34	S (E_{22}^S)	1.39	S (E_{22}^S) or M (E_{11}^M)	1.46	S (E_{22}^S) or M (E_{11}^M)
d	210	1.08	S (E_{22}^S)	1.11	S (E_{22}^S)	1.18	S (E_{22}^S)
e	218	1.04	S (E_{22}^S)	1.07	S (E_{22}^S)	1.14	S (E_{22}^S)
f	230	0.99	S (E_{22}^S)	1.01	S (E_{22}^S)	1.08	S (E_{22}^S)
g	237	0.96	S (E_{22}^S)	0.98	S (E_{22}^S)	1.05	S (E_{22}^S)
h	261	0.87	S (E_{22}^S) or S (E_{11}^S)	0.89	(9,4) S (E_{22}^S)	0.95	S (E_{22}^S)
i	270	0.84	S (E_{11}^S)	0.85	(11,0) S (E_{11}^S)	0.92	S (E_{22}^S)
j	303	0.75	(8,3) or (9,1) S (E_{11}^S)	0.76	(8,3) or (9,1) S (E_{11}^S)	0.82	S (E_{11}^S)

S=semiconducting, M=metallic

Label	Raman Shift (cm^{-1})	Diameter (nm)	Assignment	Comments
E_{LASER} = 514 nm (2.41 eV)				
I	~1565 cm^{-1}	~1.23 nm?	S	Corresponds to peak *g*
II	1572 cm^{-1}	1.60 nm	S	Corresponds to peak *d*
E_{LASER} = 532 nm (2.33 eV)				
I	~1499 cm^{-1}	~0.94 nm	M	Corresponds to peaks *i*, *j*
II	~1521 cm^{-1}	~1.06 nm	M	Corresponds to peak *g*
III	~1542 cm^{-1}	~0.80 nm	S	Peaks 1542 cm^{-1} and 1545 cm^{-1} correspond to peaks *m* and *l*, respectively
IV	~1565 cm^{-1}	~1.25 nm	S	Peaks 1565 cm^{-1} and 1567 cm^{-1} correspond to peaks *e* (*d*) and *c* (*b*), respectively
E_{LASER} = 633 nm (1.96 eV)				
I	~1558 cm^{-1}	~1.04 nm	S	Corresponds to peak *e*
E_{LASER} = 785 nm (1.58 eV)				
I	~1542 cm^{-1}	~0.80 nm (~1.27 nm)	S(M)	Corresponds to peaks *i* and *j*?
II	~1565 cm^{-1}	~1.3 nm	S	Peak 1561 cm^{-1} corresponds to peak *d*

Table S4. G- band assignments

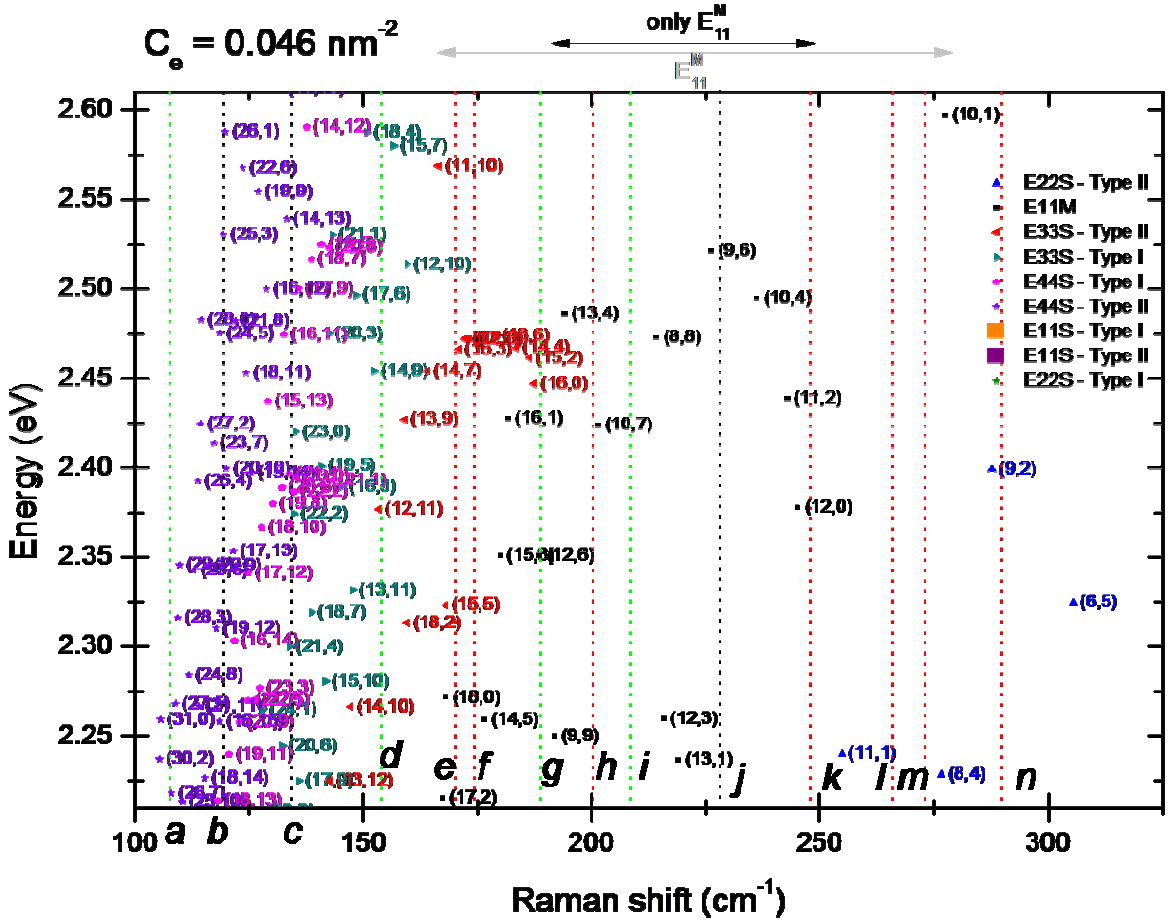

Figure S12. Kataura plot frequencies for E_{LASER} = 514 nm calculated using the expression $\omega_{RBM} = (227/d_t)\sqrt{1 + C_e \cdot d_t^2}$, where C_e = 0.046 nm^{-2}. Different (n,m) values are present. Only diameters larger than 0.7 nm are shown. Dotted lines represent observed RBMs shown in Figure S11(a). Points are labelled by the band they originate in. Semiconducting, metallic and mixed regions are delineated with respect to the labels along the top axis, indicating the band of origin (e.g. E_{11}^M is metallic, E_{22}^S is semiconducting) along the top horizontal axis.

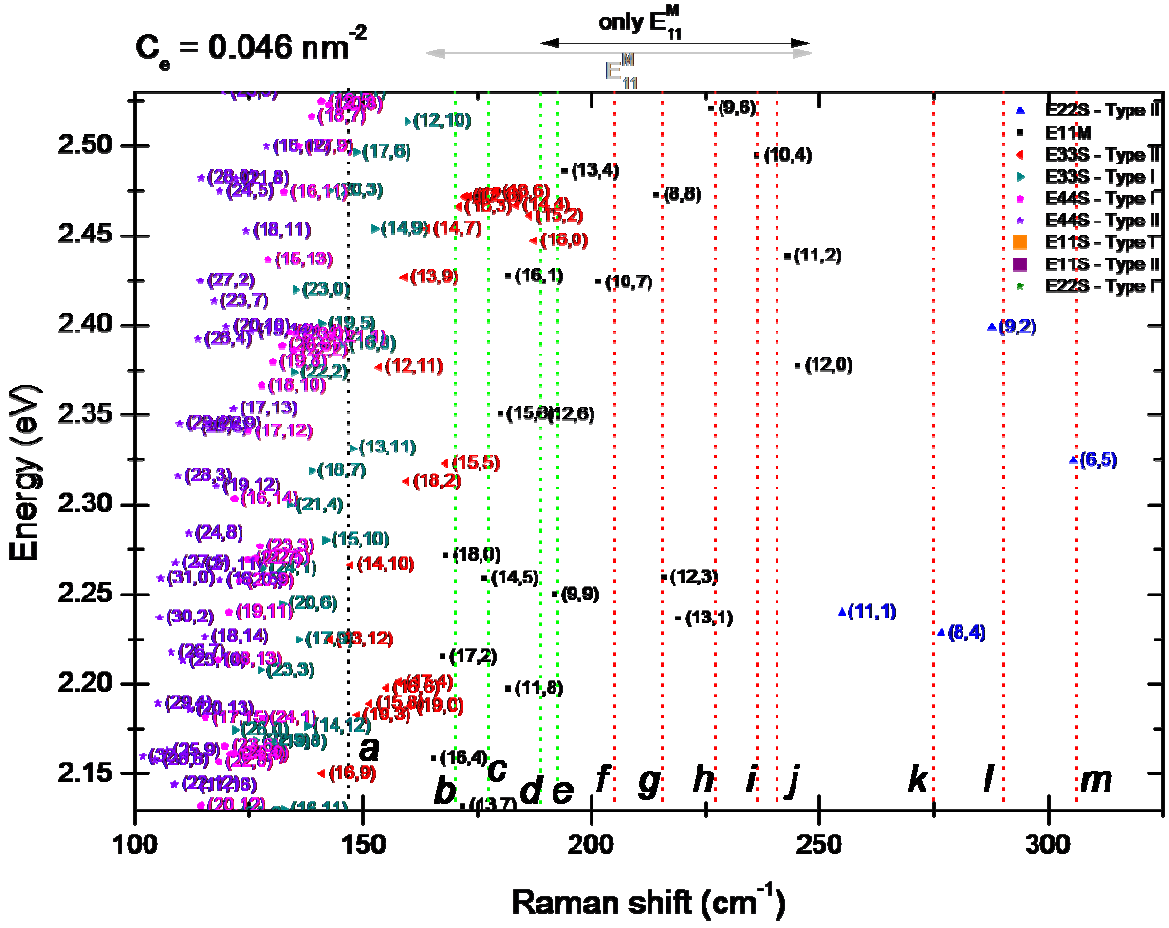

Figure S13. Kataura plot frequencies for E_{LASER} = 532 nm calculated using the expression $\omega_{RBM} = (227/d_t)\sqrt{1 + C_e \cdot d_t^2}$, where C_e = 0.046 nm^{-2}. Different (n,m) values are present. Only diameters larger than 0.7 nm are shown. Dotted lines represent observed RBMs shown in Figure S11(b). Points are labelled by the band they originate in. Semiconducting, metallic and mixed regions are delineated with respect to the labels along the top axis, indicating the band of origin (e.g. E_{11}^M is metallic, E_{22}^S is semiconducting) along the top horizontal axis.

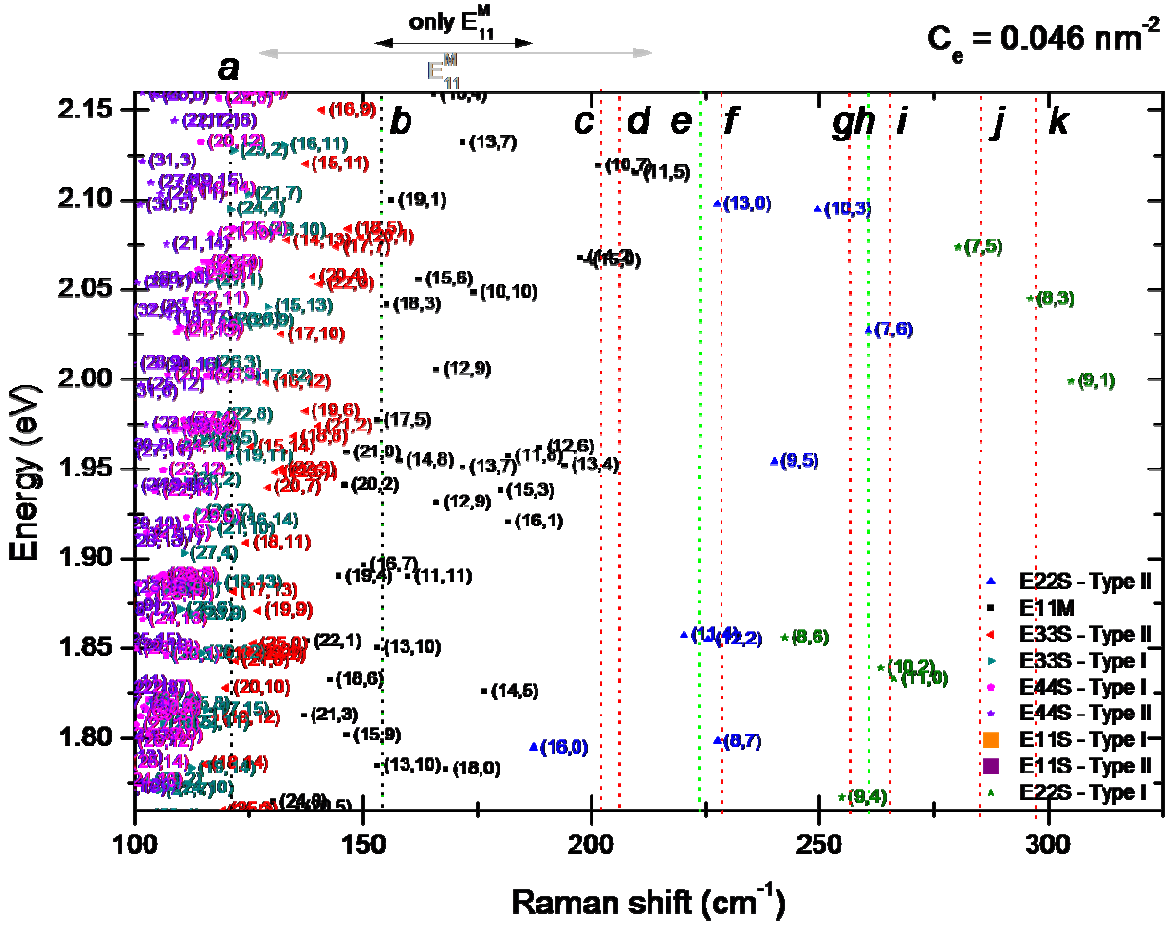

Figure S14. Kataura plot frequencies for E_{LASER} = 633 nm calculated using the expression $\omega_{RBM} = (227/d_t)\sqrt{1 + C_e \cdot d_t^2}$, where C_e = 0.046 nm^{-2}. Different (n,m) values are present. Only diameters larger than 0.7 nm are shown. Dotted lines represent observed RBMs shown in Figure S11(c). Points are labelled by the band they originate in. Semiconducting, metallic and mixed regions are delineated with respect to the labels along the top axis, indicating the band of origin (e.g. E_{11}^M is metallic, E_{22}^S is semiconducting) along the top horizontal axis.

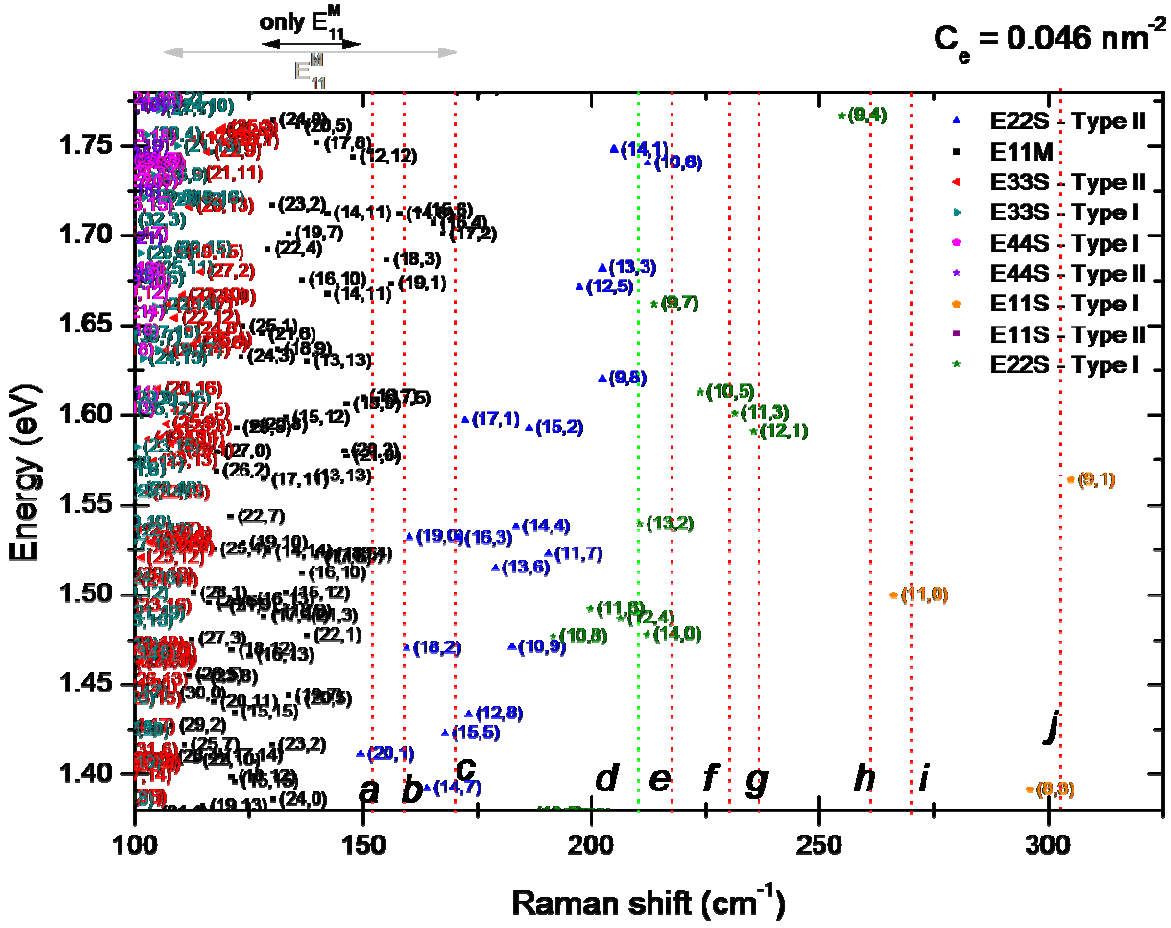

Figure S15. Kataura plot frequencies for E_{LASER} = 785 nm calculated using the expression $\omega_{RBM} = (227/d_t)\sqrt{1 + C_e \cdot d_t^2}$, where C_e = 0.046 nm^{-2}. Different (n,m) values are present. Only diameters larger than 0.7 nm are shown. Dotted lines represent observed RBMs shown in Figure S11(d). Points are labelled by the band they originate in. Semiconducting, metallic and mixed regions are delineated with respect to the labels along the top axis, indicating the band of origin (e.g. E_{11}^M is metallic, E_{22}^S is semiconducting) along the top horizontal axis.

8. Background correction illustration

For a given peak, the integrated peak area is obtained by subtracting the trapezoidal baseline. See Figure S16 and ref. 15 for a complete description.[16]

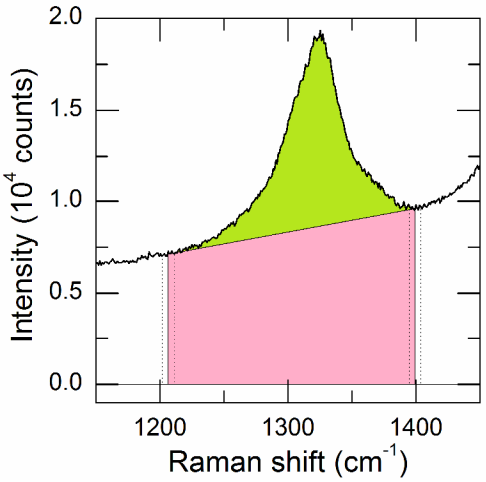

Figure S16. Integrated area (green) and baseline trapezoid (pink) are shown for typical D band at T = 350 °C.

9. Comparison of D band lineshape

Figure S17 shows typical D band spectra before and after etching at room temperature, and during etching at T = 550 °C at different times, with all D band intensities normalized to 1. The sample was etched in air for 42 minutes.

Apart from signal loss incurred from the destruction of sp^3 carbon, there is no clear change in D band structure throughout the entire etching process.

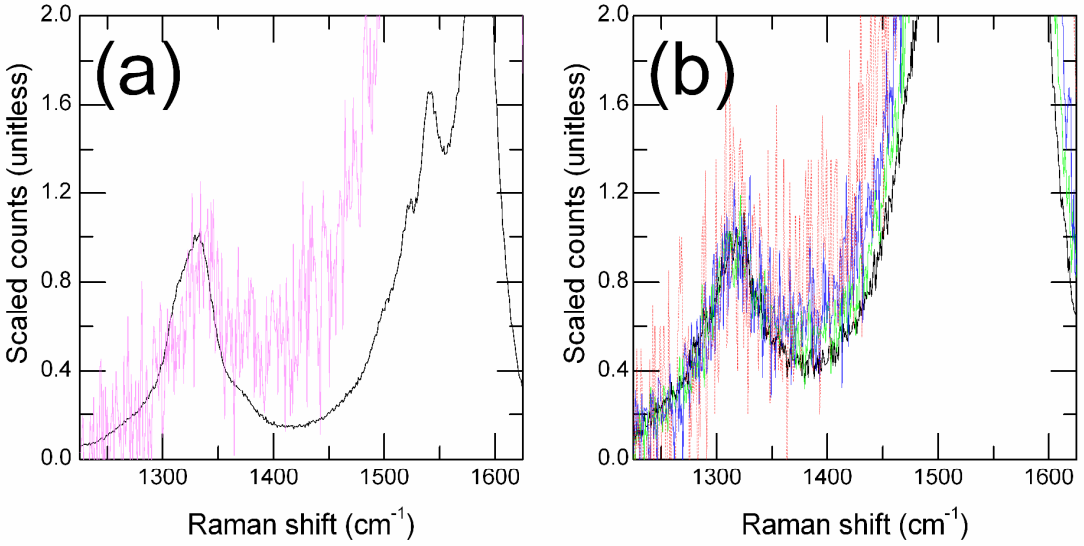

Figure S17. (a) Scaled D band at room temperature before (black) and after etching (magenta). (b) Scaled D band during air etching at T = 550 °C for etching times t = 0 (black), t = 3 min (green), t = 6 min (blue), and t = 12 min (red).

10. XPS spectra

The X-ray photoelectron spectroscopy (XPS) spectrum of a typical pre-etch sample was taken using a PHI 5500 system with an aluminum x-ray source, as shown in Figure S16. The asymmetric peak at ~ 284.3 eV corresponds to the 1s photoelectron line of carbon, typical of sp^2 hybridization.[17-20] The peak is relatively narrow (i.e. full width at half maximum is ~0.92 eV) with no pronounced doublet structure, suggesting that sp^3 content is low compared to sp^2 content. This is consistent with the presence of CNTs with relatively few defects and a low amount of amorphous carbon.[17-20]

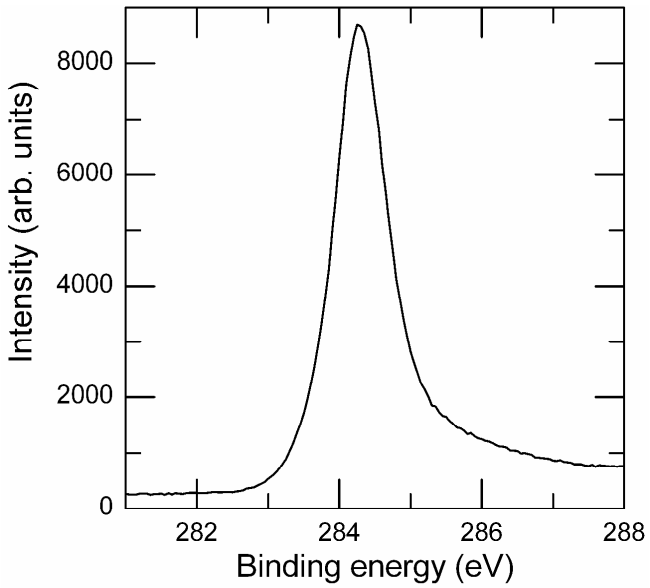

Figure S18. XP spectrum of the C 1s region for a pre-etch sample.

REFERENCES

1. Nugraha, A. R. T.; Saito, R.; Sato, K.; Araujo, P. T.; Jorio, A.; Dresselhaus, M. S. Dielectric Constant Model for Environmental Effects on the Exciton Energies of Single Wall Carbon Nanotubes. *Appl. Phys. Lett.* **2010***, 97*, 091905-3.

2. Sato, K.; Saito, R.; Jiang, J.; Dresselhaus, G.; Dresselhaus, M. S. Discontinuity in the Family Pattern of Single-Wall Carbon Nanotubes. *Phys. Rev. B* **2007***, 76*, 195446.

3. Telg, H.; Duque, J. G.; Staiger, M.; Tu, X.; Hennrich, F.; Kappes, M. M.; Zheng, M.; Maultzsch, J.; Thomsen, C.; Doorn, S. K. Chiral Index Dependence of the G+ and G- Raman Modes in Semiconducting Carbon Nanotubes. *ACS Nano* **2012***, 6*, 904-911.

4. Araujo, P. T.; Pesce, P. B. C.; Dresselhaus, M. S.; Sato, K.; Saito, R.; Jorio, A. Resonance Raman Spectroscopy of the Radial Breathing Modes in Carbon Nanotubes. *Phys. E* **2010***, 42*, 1251-1261.

5. Saito, R.; Fantini, C.; Jiang, J. In *Excitonic States and Resonance Raman Spectroscopy of Single-Wall Carbon Nanotubes;* Jorio, A., Dresselhaus, G. and Dresselhaus, M. S., Eds.; **Carbon Nanotubes: Advanced Topics in the Synthesis, Structure, Properties and Applications (Topics in Applied Physics)**; Springer-Verlag Berlin Heidelberg: Berlin, 2008; Vol. 111, pp 251.

6. Fantini, C.; Jorio, A.; Souza, M.; Strano, M. S.; Dresselhaus, M. S.; Pimenta, M. A. Optical Transition Energies for Carbon Nanotubes from Resonant Raman Spectroscopy: Environment and Temperature Effects. *Phys. Rev. Lett.* **2004***, 93*, 147406.

7. Bachilo, S. M.; Strano, M. S.; Kittrell, C.; Hauge, R. H.; Smalley, R. E.; Weisman, R. B. Structure-Assigned Optical Spectra of Single-Walled Carbon Nanotubes. *Science* **2002***, 298*, 2361-2366.

8. Araujo, P. T.; Fantini, C.; Lucchese, M. M.; Dresselhaus, M. S.; Jorio, A. The Effect of Environment on the Radial Breathing Mode of Supergrowth Single Wall Carbon Nanotubes. *Appl. Phys. Lett.* **2009***, 95*, 261902-3.

9. Jorio, A.; Souza Filho, A. G.; Dresselhaus, G.; Dresselhaus, M. S.; Swan, A. K.; Unlu, M. S.; Goldberg, B. B.; Pimenta, M. A.; Hafner, J. H.; Lieber, C. M.*, et al.* G-Band Resonant Raman Study of 62 Isolated Single-Wall Carbon Nanotubes. *Phys. Rev. B* **2002***, 65*, 155412.

10. Dresselhaus, M. S.; Jorio, A.; Hofmann, M.; Dresselhaus, G.; Saito, R. Perspectives on Carbon Nanotubes and Graphene Raman Spectroscopy. *Nano Lett.* **2010***, 10*, 751-758.

11. Bachilo, S. M.; Balzano, L.; Herrera, J. E.; Pompeo, F.; Resasco, D. E.; Weisman, R. B. Narrow (n,m)-Distribution of Single-Walled Carbon Nanotubes Grown using a Solid Supported Catalyst. *J. Am. Chem. Soc.* **2003***, 125*, 11186-11187.

12. Jorio, A.; Pimenta, M. A.; Filho, A. G. S.; Saito, R.; Dresselhaus, G.; Dresselhaus, M. S. Characterizing Carbon Nanotube Samples with Resonance Raman Scattering. *New J. Phys.* **2003***, 5*, 139.

13. Miyata, Y.; Kawai, T.; Miyamoto, Y.; Yanagi, K.; Maniwa, Y.; Kataura, H. Chirality-Dependent Combustion of Single-Walled Carbon Nanotubes. *J. Phys. Chem. C* **2007***, 111*, 9671-9677.

14. Kawai, T.; Miyamoto, Y. Chirality-Dependent C-C Bond Breaking of Carbon Nanotubes by Cyclo-Addition of Oxygen Molecule. *Chem. Phys. Lett.* **2008***, 453*, 256-261.

15. Dresselhaus, M. S.; Dresselhaus, G.; Saito, R.; Jorio, A. Raman Spectroscopy of Carbon Nanotubes. *Phys. Rep.* **2005***, 409*, 47-99.

16. Li-Pook-Than, A.; Lefebvre, J.; Finnie, P. Phases of Carbon Nanotube Growth and Population Evolution from *in Situ* Raman Spectroscopy during Chemical Vapor Deposition. *J. Phys. Chem. C* **2010***, 114*, 11018-11025.

17. Haerle, R.; Riedo, E.; Pasquarello, A.; Baldereschi, A. Sp^{2}/sp^{3} Hybridization Ratio in Amorphous Carbon from C 1s Core-Level Shifts: X-Ray Photoelectron Spectroscopy and First-Principles Calculation. *Phys. Rev. B* **2001***, 65*, 045101.

18. Nikitin, A.; Ogasawara, H.; Mann, D.; Denecke, R.; Zhang, Z.; Dai, H.; Cho, K.; Nilsson, A. Hydrogenation of Single-Walled Carbon Nanotubes. *Phys. Rev. Lett.* **2005***, 95*, 225507.

19. Kundu, S.; Wang, Y.; Xia, W.; Muhler, M. Thermal Stability and Reducibility of Oxygen-Containing Functional Groups on Multiwalled Carbon Nanotube Surfaces: A Quantitative High-Resolution XPS and TPD/TPR Study. *J. Phys. Chem. C* **2008***, 112*, 16869-16878.

20. Estrade-Szwarckopf, H. XPS Photoemission in Carbonaceous Materials: A "Defect" Peak Beside the Graphitic Asymmetric Peak. *Carbon* **2004***, 42*, 1713-1721.